frontiers | Frontiers in Earth Science

TYPE Original Research
PUBLISHED 26 March 2025
DOI 10.3389/feart.2025.1507580

OPEN ACCESS

EDITED BY
Zhangdong Jin,
Institute of Earth Environment, Chinese Academy of Sciences (CAS), China

REVIEWED BY
Zhanping Song,
Xi'an University of Architecture and Technology, China
Jiang Hai Yang,
China University of Geosciences Wuhan, China

*CORRESPONDENCE
Feng Guo,
guofengt@263.net

RECEIVED 09 October 2024
ACCEPTED 10 March 2025
PUBLISHED 26 March 2025

CITATION
Huang X, Guo F, Zhao L and Zhang F (2025) Chemical weathering records in Yungang Formation, North China: implications for stone heritage conservation.
Front. Earth Sci. 13:1507580.
doi: 10.3389/feart.2025.1507580

Chemical weathering records in Yungang Formation, North China: implications for stone heritage conservation

Xin Huang[1,2], Feng Guo[1,2,3]*, Liang Zhao[1,3] and Feng Zhang[1,2]

[1]State Key Laboratory of Isotope Geochemistry, Guangzhou Institute of Geochemistry, Guangzhou, China, [2]College of Earth and Planetary Sciences, University of Chinese Academy of Sciences, Beijing, China, [3]College of Resources and Environment, Yangtze university, Wuhan, China

The Yungang Grottoes located in Datong area, North China, have experienced extensive surface and structural damage. Previous studies have recognized the importance of temperature and water during weathering, but the quantitative evaluation on both the physical and chemical weathering remains absent. Here we conducted geochemical analyses on the sculpture-hosting sedimentary rocks of Shiku Member in Jurassic Yungang Formation. The results reveal that feldspar dissolution is predominant during chemical weathering, while the effects caused by other factors like calcic cement and sulphate are minor. The estimated chemical weathering rate of feldspar is 7.84×10^{-21} - 2.7×10^{-18} mol·cm^{-2}·s^{-1}, with an average cumulative chemical weathering amount of 1.46×10^{-11} mol·cm^{-2}·y^{-1}. The mass loss caused by chemical weathering is about 0.000061% per year and the annual mass loss rate is approximately 0.00015%–0.00018% when the effect of physical weathering is considered. The damage (5% mass loss) of Yungang Grottoes (450–520 AD) began in ca. AD 800 and all grottoes will be destroyed in the upcoming 4,000–5,000 years without protection. As the chemical weathering of feldspar is controlled by local temperature change, the grottoes should be accommodated in relatively constant low-temperature environment through adding eaves and air conditioners.

KEYWORDS

Yungang Grottoes, chemical weathering, temperature, heritage conservation, North China

1 Introduction

Grottoes are common stone heritages that provide valuable records of the contemporaneous social environment, production activities, transformation and utilization of nature, religious customs and other social conditions (Gomez-Heras and McCabe, 2015; Li et al., 2014; Ponziani et al., 2012). The diverse grottoes hold crucial clues to explore historical truths and preserving unique historical, scientific, cultural, social, economic, and artistic values (Guo and Bai, 2024).

The Yungang Grottoes, located on Wuzhou Mountain in Datong area of Shanxi Province, have existed for 1,500 years and attract thousands of tourists every year (Shao et al., 2024). Historical records suggest that there might be 100,000 stone Buddhas across the Yungang Grottoes (Wang et al., 2014). However, since the grottoes are large and difficult to move,

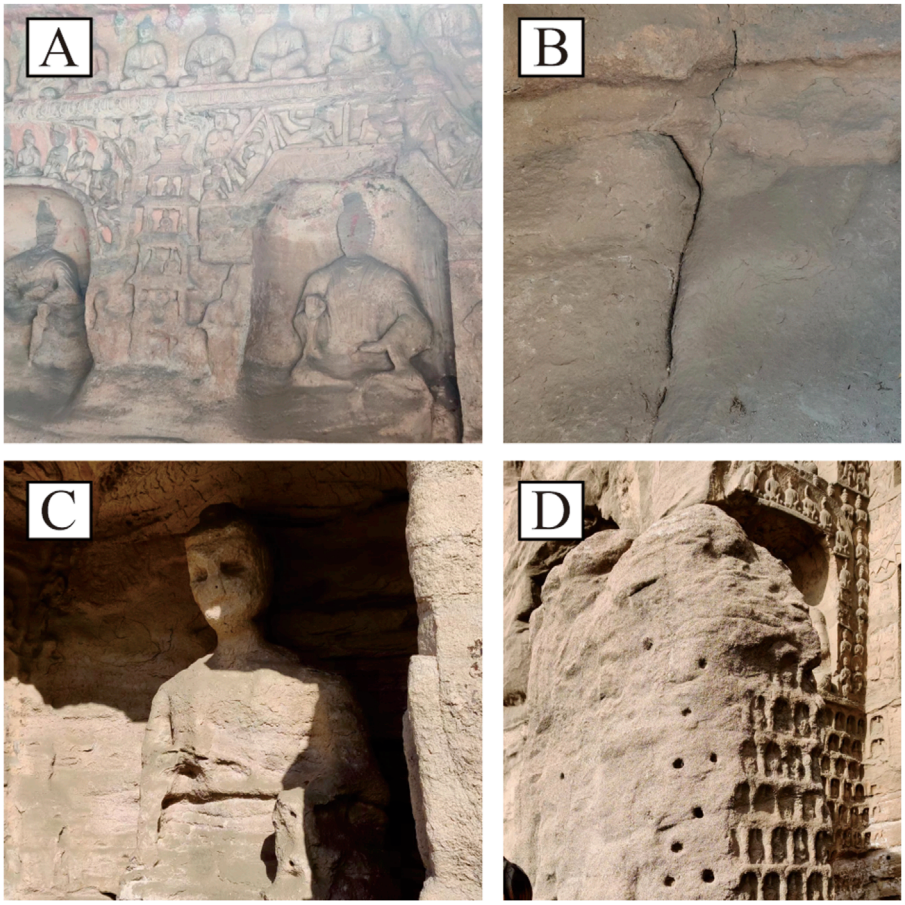

FIGURE 1
Current weathering states present in the Yungang Grottoes. **(A)** Collapse, **(B)** cracking and **(C, D)** shedding.

they have been significantly affected by natural environments and human activities over a long period (Zhang et al., 2022), resulting in surface weathering and structural damage, e.g., cracking, collapse and shedding (Figure 1) (Guo and Jiang, 2014). Thousands of statues have been lost due to increasing damage by natural weathering, making it necessary for immediate protection.

The weathering processes include physical and chemical weathering. On the one hand, physical weathering refers to the process of rock disintegration and fragmentation into debris and particles of various sizes due to physical and mechanical forces. There has been significant damage caused by physical weathering in the Yungang Grottoes. Cracks in the grottoes have been detected using various methods since the last century (Huang and Zhang, 1998), which provide a pathway for rainwater infiltration, posing a significant obstacle to the preservation efforts of the Yungang Grottoes. The local climate is characterized by concentrated rainfall in summer, rainwater is also within the category of physical weathering (Camuffo, 1995). In addition, frequent and cyclic temperature variations induce the development and expansion of pores and cracks, thereby accelerating the degradation and weathering processes of rock in the grotto temples (Vlcko et al., 2009; Xia et al., 2024). When the temperature decreases, condensation water forms and leads to the degradation of the Yungang Grottoes (Huang et al., 2022). Furthermore, dust deposition and black soot stains appear in multiple grottoes, significantly affecting the weathering resistance and aesthetic value (Liu et al., 2011). Finally, the southern flanks of grottos, more frequently exposed to sunlight, show greater intensity of weathering than the northern flanks (Ren et al., 2019). On the other hand, chemical weathering refers to the process in which rocks undergo compositional change and form new substances under the influence of various factors such as water, carbon dioxide, SO_2 and oxygen. Destruction caused by chemical weathering, such as salt crystallization, calcite deposition and kaolinization of feldspar (Fu et al., 2009; Yuan and Feng, 2004), is also commonly observed, including Grottoes No. 41 and No. 45 (Liu et al., 2011).

Previous studies have widely recognized that temperature and water play crucial roles in both the physical and chemical weathering processes of grottoes (Becherini et al., 2010; Li et al., 2019; Paradise, 2002; Ponziani et al., 2012; Warscheid and Braams, 2000; Yan et al., 2007). For instance, temperature and humidity influence the formation of condensation water, freeze-thaw cycles, and ice wedging (Ponziani et al., 2012; Xia et al., 2024; Yang et al., 2018; Zhou et al., 2023). Moreover, low pH value of water accelerates the chemical weathering in the Yungang Grottoes (Bastien et al., 2016; Zhang et al., 2009). Nevertheless, the quantitative evaluation of both

physical and chemical weathering on the Yungang Grottoes remains absent, making it difficult to accurately implement protection measures and extend the life of these stone heritages. The dissolution rate of minerals (such as feldspar and calcite) in solution can be used to quantitatively estimate the intensity and timescale of chemical weathering (Burch et al., 1993; Crundwell, 2015a; Crundwell, 2015b; Steefel and Cappellen, 1990). The Yungang Grottoes are just engraved on the sedimentary rocks (mainly feldspar-quartz sandstones) of Shiku Member (here Member refers to a lithostratigraphic unit) in the Jurassic Yungang Formation and show extensive chemical weathering. We therefore conduct geochemical analyses (mineralogy and chemical compositions) on 19 samples of sedimentary rocks from the Shiku Member (lithostratigraphic unit). The aims of this study are focused on the main factors influencing the chemical weathering and estimation of the weathering rate in accordance with the local climate data. The results have potential for developing targeted recommendations and evaluating protection strategies, and for reducing the weathering of the Yungang Grottoes.

2 Methods and materials

2.1 Material sampling

The Yungang Grottoes are located in the southern foothills of Wuzhou Mountain, about 16 km west of Datong City, Shanxi Province, North China, with a geographical location of 113°20′E and 40°04′N. The Datong area has a temperate continental monsoon climate, with average annual rainfall of 330 mm (Yuan and Feng, 2004). The grottoes are excavated on the sandstones of Shiku Member (lithostratigraphic unit) of Yungang Formation (Figure 2) (Fan et al., 2014; Shao et al., 2024). The mineral composition of Yungang grottoes mainly includes quartz, feldspar, calcite, with accessory clay minerals and sulfate. The sulfate is usually associated with calcite on the surface of the sandstones, representing the reacted product between the atmospheric SO_2, vapor and calcite (Liu et al., 2011; Zhang et al., 2023). There are 45 main caves and 209 affiliated caves, with a carving area of more than 18,000 square meters. There are more than 1,100 Buddhist niches and more than 59,000 statues (Ma et al., 2005; Zhang et al., 2023).

We collected 19 samples (Nos. 19YG-01 to 19YG-19) from bottom to top (Figure 2C) of a profile (113°15′E, 40°11′N) of Shiku Member (lithostratigraphic unit) located about 3 km east of the Yungang Grottoes (Ai et al., 2021). The sedimentary profile exhibits nearly horizontal layers with very low dip angles (<10°, Figure 2C), showing minimal deformation and indicating a relatively tectonically stable setting since the Middle Jurassic (Taherynia et al., 2016; Zhou et al., 2017). The color, grain size, and lithology in the profile are completely identical to those sedimentary strata where the Yungang Grottoes are carved (Figure 2C).

2.2 Analytical techniques

The bulk-rock major and trace element contents were analyzed at Tongwei Analytical Technology Co., Ltd., in Guiyang, China. The fresh samples were cut and finely ground to powders of <200 mesh. For major element analysis, approximately 0.5 g of the powdered sample were dried at 105°C for at least 2 h to remove the adsorbed water, and then these samples were mixed with with 3.6 g of $Li_2B_4O_7$, 0.4 g of LiF, 0.3 g of NH_4NO_3, and a small amount of LiBr in a platinum crucible. This mixture was then melted in a furnace to create a glass disk. Major oxide concentrations were determined using ARL Perform 'X 4200 X-ray fluorescence (XRF) spectrometer produced by Thermo Fisher. The standard samples GSR-1 (granite), GSR-2 (andesite), and GSR-3 (basalt) were repeatedly analyzed to obtain consistent results, with analytical errors within 2% (Fan et al., 2004; Wen et al., 2024).

During trace element analysis, approximately 0.1 g powder was digested in a mixture of 1 mL HNO_3 and 0.5 mL HF within high-pressure Teflon bombs. Steel-jacketed bombs were used for the digestion process, being placed in an oven at 195°C for 2 days to ensure complete digestion. Once cooled, the bombs were opened, and the contents were dried on a hotplate. They were then re-dissolved with 5 mL of 15 wt% HNO_3 and 1 mL of Rh internal standard, sealed, and placed in an oven at 150°C overnight. Aliquots of the digested solutions, diluted by a factor of 2000, were nebulized into an Agilent Technologies 7,700x quadrupole ICP-MS for trace element analysis. Repeated analysis of W-2a (diabase) and BHVO-2 (basalt) yields an analysis error of ≤5% (Liu et al., 1996; Wei et al., 2022).

To further determine the mineral compositions of the sedimentary rocks in the Shiku Member (lithostratigraphic unit), we selected 1-3 samples from each lithology for X-ray diffraction (XRD) analysis (Li et al., 2018; Li et al., 2019). The XRD analyses were also conducted at Guangzhou Tuoyan Testing Co., Ltd. About 0.5 g sample powder is set into the groove of microprobe slide and then is analyzed by a D8ADVANCE X-ray diffractometer (Bruker, Germany) at room temperature with a relative humidity of 50%. The test adheres to the SY/T 5163–2010 standard. The instrumental conditions include a Cu target, a voltage of 40 kV and a current of 100 mA for the X-ray tube, scanning width to 0.02° (2θ), and a step time of 1 s. The original data of XRD analyses are listed in Supplementary Table S1.

The particle size of the sample was investigated using a polarizing microscope. The grain size of terrigenous debris was determined according to the Udden-Wentworth grain size standard. Moreover, alizarin red S was used for staining to enhance the observations (the calcite shows red).

3 Results and discussion

3.1 Mineral compositions of the Shiku Member

The studied samples (from 19YG-01 to 19YG-19) are mainly composed of quartz (Qtz), plagioclase (PL), K-feldspar, calcite (Cal) and clay minerals (Figure 3) with a small amount of accessory dolomite and hematite. These minerals have angular shapes, showing the characteristics of near-source deposition (Kovach et al., 2023).

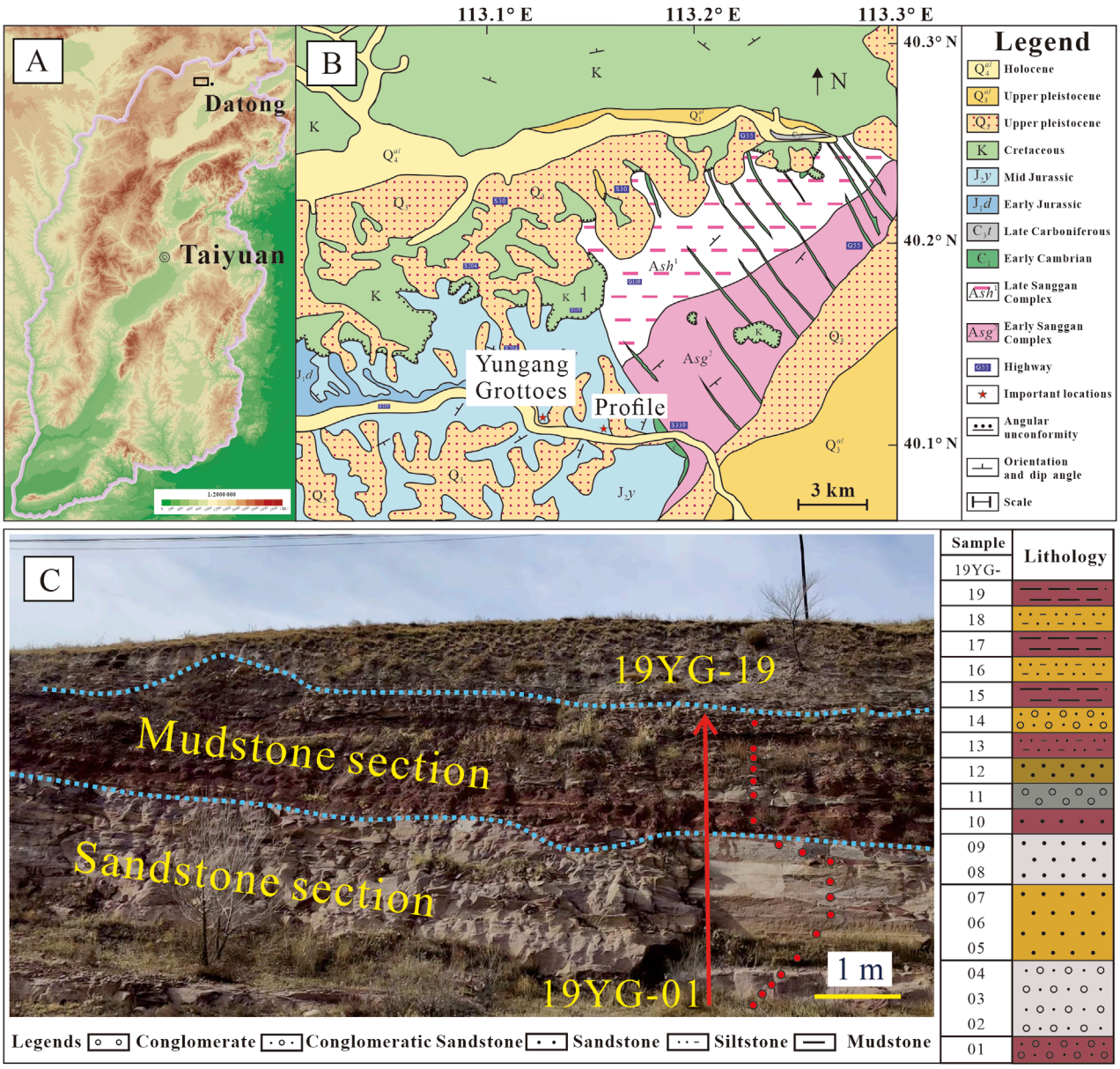

FIGURE 2
The geographic and geological maps showing the sampling locations and profile in Datong area, North China. **(A)** The geographic map, **(B)** the geological map, **(C)** the field profile showing the lithological column of the Shiku Member of Yungang Formation.

As illustrated in Figure 4, the XRD results (Table 1) obtain the main mineral components of the 10 samples in the Shiku Member (Figures 5B–E). The lithology of the sample (Figure 5A) is strongly correlated with the particle size. The main minerals of sandstone include quartz (35.2%–48.1%, average of 42.0%), K-feldspar (13.2%–25.0%, average of 18.1%), plagioclase (11.7%–20.8%, average of 14.1%), calcite (3.9%–23.5%, average of 13.4%) and clay minerals (7.0%–12.8%, average of 9.7%). The mineral phases of mudstone are obviously different from those of sandstone, including quartz (34.3%–56.2%, average of 46.1%), K-feldspar (0%–22.0%, average of 11.6%), plagioclase (5.1%–11.7%, average of 7.3%), and clay minerals (14.6%–30.3%, average of 23.4%), with little or even no carbonate found. The whole section contains very little dolomite and hematite.

3.2 Chemical weathering index of the Shiku Member

The chemical index of alteration (*CIA*) is extensively utilized to assess the weathering intensity of samples (Nesbitt and Young, 1982). The *CIA* is calculated based on the oxide content to assess the degree of transformation from feldspar minerals to clay minerals. The formula for *CIA* is as Equation 1:

$$CIA = [Al_2O_3/(Al_2O_3 + CaO* + Na_2O + K_2O)] \times 100 \quad (1)$$

The oxide contents used in the calculations are derived from the XRF results. CaO^* represents the Ca content in the silicate component (excluding nonsilicate materials such as carbonates and

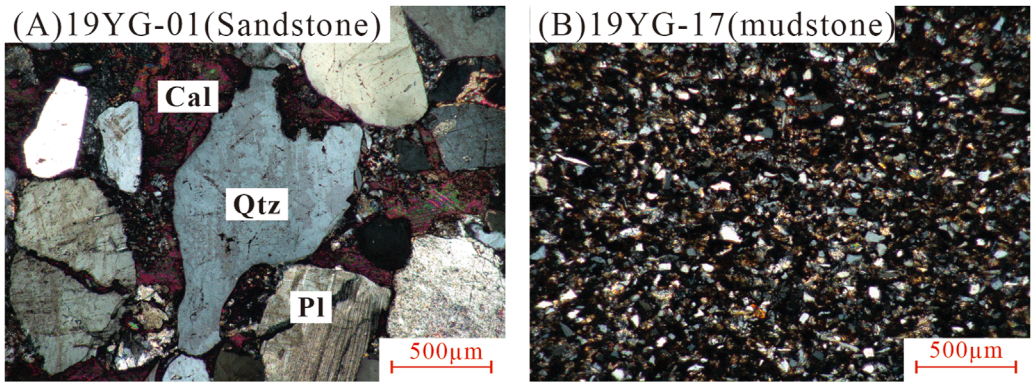

FIGURE 3
The mineralogical characteristics of representative sandstone **(A)** and mudstone samples **(B)** of the Shiku Member under microscope (Mineral abbreviations: Qtz - Quartz, Pl - Plagioclase, Cal - Calcite).

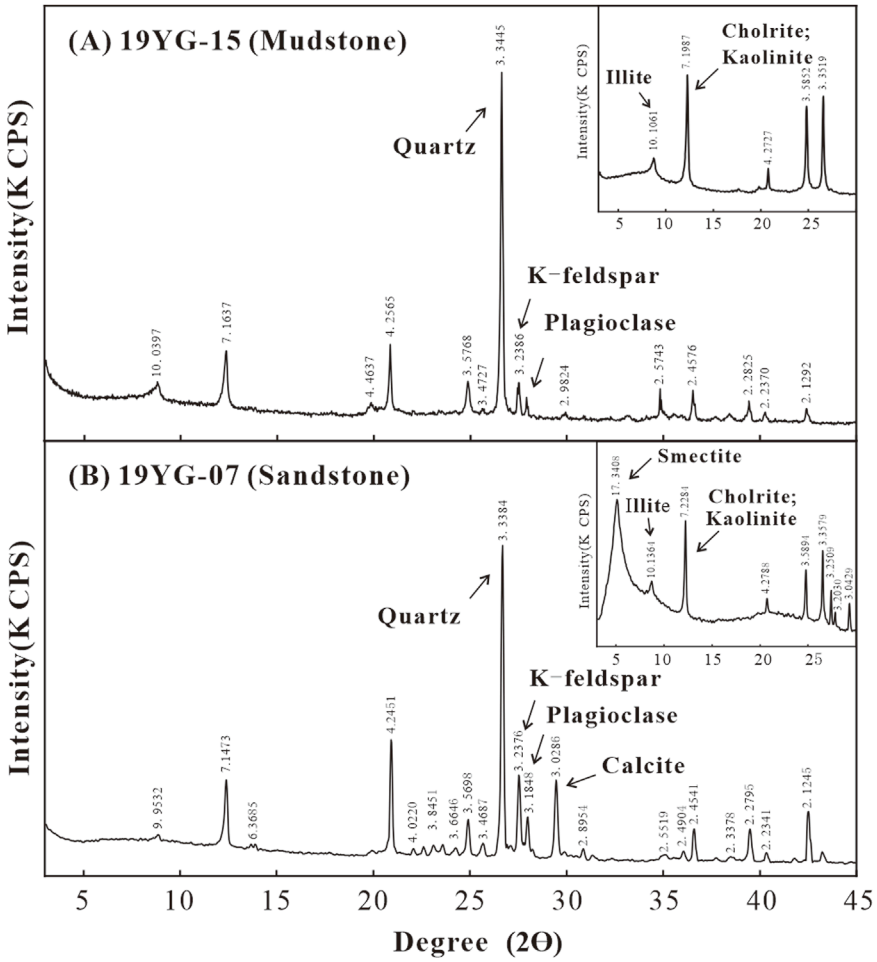

FIGURE 4
The XRD patterns of representative mudstone **(A)** and sandstone samples **(B)** of the Shiku Member.

phosphates). McLennan et al. (1993) proposed an indirect method to calculate CaO^*. They introduced a parameter of $CaO_{Residual} = CaO - (10/3 \times P_2O_5)$; if $CaO_{Residual} < Na_2O$, then $CaO^* = CaO_{Residual}$; if $CaO^* > Na_2O$, then $CaO^* = Na_2O$ (McLennan et al., 1993). All oxides are expressed as molar fractions during the calculation.

According to Formula 1, the *CIA* values of the Shiku Member (lithostratigraphic unit) range from 59.7 to 85.9, with an

10.3389/feart.2025.1507580

TABLE 1 The XRD results of samples from the Shiku Member.

Sample	Lithology	Quart%	K-feldspar	Plagioclase%	Calcite%	Clay%	Dolomite%	Hematite%
19YG-01	Conglomeratic Sandstone	35.4	17.7	14.0	19.8	9.6	1.8	1.7
19YG-03		48.1	16.5	14.7	3.9	12.8	1.8	2.2
19YG-04		41.9	13.9	12.0	23.5	7.0	1.7	0
19YG-06	Sandstone	44.1	25.0	13.0	4.4	10.1	1.9	1.5
19YG-07		35.2	24.3	12.2	16.6	9.4	2.3	0
19YG-09		41.3	13.2	20.8	10.6	11.7	2.4	0
19YG-11	Conglomerate	47.8	16.4	11.7	14.8	7.0	2.3	0
19YG-13	Siltstone	34.3	22.0	5.1	21.3	14.6	2.7	0
19YG-15	Mudstone	47.9	12.8	5.2	0	30.3	0.7	3.1
19YG-19		56.2	0	11.7	0	25.3	1.6	5.2

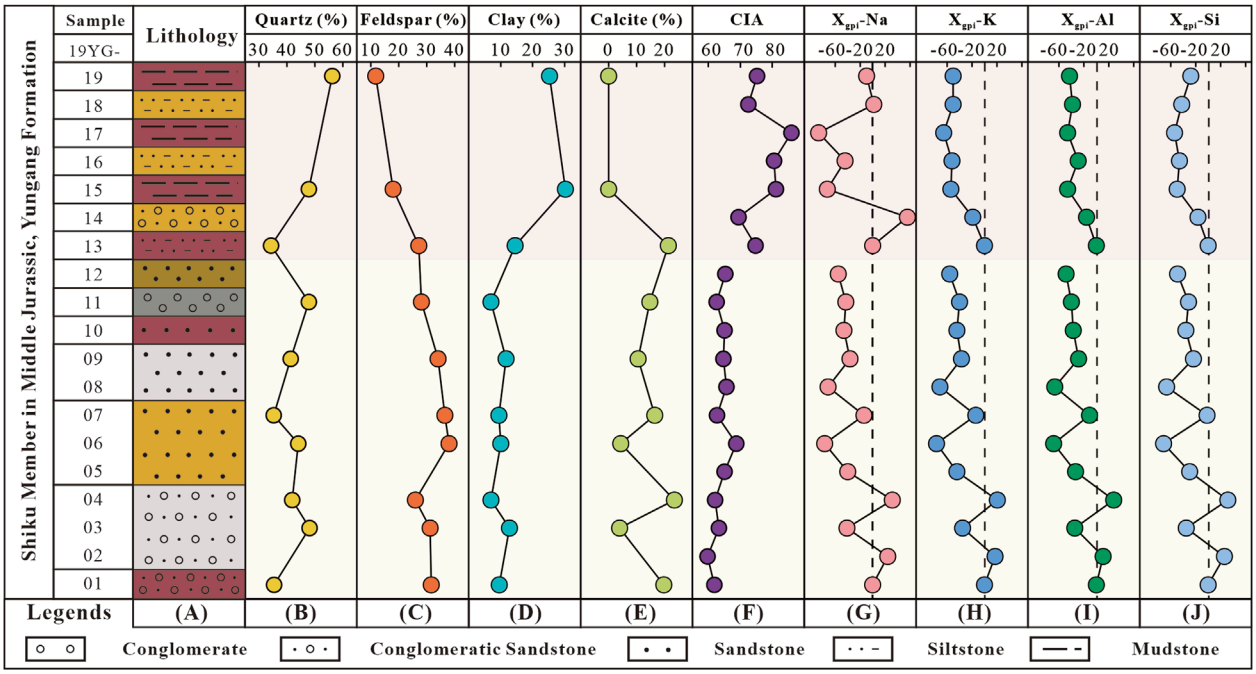

FIGURE 5
Diagrams showing the mineral compositional variations and elemental migration trends in the profile. **(A)** The columnar sampling profile, vertical mineral compositional variations **(B)** quartz; **(C)** feldspar; **(D)** clays; **(E)** calcite; **(F)** *CIA* change), and X_{gpi} variation profiles **(G)** Na; **(H)** K; **(I)** Al; and **(J)** Si) of the Shiku Member.

average of 68.7 (Figure 5F). Notably, there is a significant *CIA* shift between 19YG-12 and 19YG-13, which corresponds to a change in grain size and lithology. Most of these samples from 19YG-01 to 19YG-12 are sandstones, which exhibit lower *CIA* values (59.7–68.8, with an average of 64.1), while the samples from 19YG-13 to 19YG-19 are mostly mudstones, which have higher *CIA* values (69.4–86, with an average of 77.4). Based on the weathering intensity indicated by the *CIA* value, we roughly subgroup the profile into sandstone section and mudstone section. The sandstone section includes the samples from 19YG-01 to 19YG-12 and the samples of 19YG-13 to 19YG-19 in the mudstone section. It should be noted that there are sandstones interbedded in the mudstone section; similarly, some mudstones are interbedded in the sandstone section.

3.3 The elemental migration trends

The weathering of rocks is often accompanied by elemental migration. The "mobile element" refers to that with obvious compositional change during weathering, whereas the "immobile element" represents that with little or no variation (Ng et al., 2001). Nevertheless, the mobility of an element in different systems or phases may change (Gong et al., 2012; Little and Lee, 2006), e.g., Zr is generally stable and it becomes active in the case of zircon formation or decomposition (Riebe et al., 2003). Similar cases include P, which is largely controlled by apatite (Guidry and Mackenzie, 2000), Sr that is largely controlled by plagioclase (Hogarth and Robin, 2007), and also Ti, Nb and Ta, which are largely controlled by rutile and Fe-Ti oxides (Frost and Lindsley, 1991). It is therefore crucial to identify which elements are immobile in the system before we apply them to estimate the chemical weathering rate in the Shiku Member (lithostratigraphic unit). Here we adapt the plateau method proposed by Gong et al. (2011) to identity the immobile elements.

(1) Twelve elements including Ta, Nb (Frost and Lindsley, 1991), U, La, Zr (Riebe et al., 2003), Hf, Al (Pokrovsky et al., 2006), Th (Ndjigui et al., 2008), Sc (Shotyk et al., 2001), Ti (Frost and Lindsley, 1991), Yb and Y (Gong et al., 2011) were selected for consideration. Because these elements are the most common immobile elements in the weathering process.

(2) Two continuous samples from the profile (e.g., 19YG-01 and 02) are selected to calculate the concentration ratio of the same element (Supplemetnary Figure A1). We assume (a) the original composition of adjacent samples is the same; (b) the lower layer of the sample is buried deeper with less weathering degree, so it represents the original rock; and (c) from the bottom to top is regarded as a continuous weathering procedure of the original rock (Ji et al., 2004; Walter et al., 1995). Furthermore, the principle of denominator selection is to ensure that most elemental ratios are less than 1, such as in Supplemetnary Figure A1B, we use 19YG-02/19YG-03 ratio to show the relative mobility of elements.

(3) Since the contents of immobile elements in the protolith and altered rocks are theoretically identical or approximate, there is a platform in the spider diagram (Supplemetnary Figure A1, their ratios represent the mass change during weathering). Taking 19YG-02/19YG-01 as an example, Ta, Nb, La, Al, Th, Ti, Yb and Y (Black fonts in Row 3, Supplemetnary Table S1C) can be regarded as a platform. The mass ratio (*MR*) in the example is calculated as Equation 2 (Gong et al., 2011; Gong et al., 2012):

$$MR = \underset{i=1}{\overset{n}{Median}}\left(MR_i\right) = \underset{i=1}{\overset{n}{Median}}\ \left(R_w/R_p\right) \tag{2}$$

where R_p represents the weight percentage of the immobile element i in the reference sample, while R_w denotes the weight percentage of the immobile element i in the other sample, and n is the number of immobile elements determined by the plateau method. We obtain $MR = 0.84$ between 19YG-02 and 19YG-01.

(4) MR^* is the ratio of the sample to the protolith (in the sandstone section, we consider 19YG-01 as the protolith and 19 YG-13 as the protolith in the mudstone section), the MR^* of 19YG-03 = 19YG-03/19YG-01 = (19YG-03/19YG-02) × (19YG-02/19YG-01), and so on. The MR^* values of all samples are listed in Supplemetnary Table S1C. Using the obtained MR^*, the relative gain and loss of mobile elements *i* (denoted as X_{gpi}) during the weathering process can be expressed as Equation 3 (Gong et al., 2011; Ng et al., 2001):

$$X_{gpi} = 100 \times \left[\frac{\frac{R_w^i}{R_p^i}}{MR^*} - 1\right] \tag{3}$$

R_p^i represents the weight percentage of the mobile element i in the protolith, while R_w^i indicates the weight percentage of the mobile element i remaining in the weathered (or altered) product (Ng et al., 2001). According to this formula, when X_{gpi} is greater than 0, it indicates elemental migration in, and *vice versa*. We plot the change of X_{gpi} in Figures 5G–J. The X_{gpi} values in the sandstone section decrease strongly, e.g., X_{gpi}-Na changes from 31.55 to −55.26, K decreases from 20.5 to −56, X_{gpi}-Al decreases by 80, and X_{gpi}-Si also decreases from 31.7 to −49. In contrast, the X_{gpi} values for the mudstone section exhibit less variations (Figures 5G–J): the X_{gpi}-Na is about −25.9, X_{gpi}-K is approximately −48.6, X_{gpi}-Al is close to −39.5, and X_{gpi}-Si is nearly −39.5.

From the bottom to the top of the profile (19YG-01 to 19YG-19), the weathering intensity gradually increases, the contents of quartz and clay minerals gradually increase, whereas the contents of feldspar and calcite decrease. The concentrations of Na, K, Al and Si in the profile showed a decreasing trend from the bottom to the top. Such variation trends in mineral and chemical compositions can be attributed to chemical weathering of feldspar. The main reasons are listed below.

(1) Feldspar can be classified into anorthite, albite and K-feldspar (plagioclase is a solid solution formed by varying ratios of anorthite and albite), with chemical formulas of $CaAl_2Si_2O_8$, $NaAlSi_3O_8$ and $KAlSi_3O_8$ respectively. During chemical weathering, dissolution of feldspar forms clay minerals (Fu et al., 2009; Huang and Yang, 1995), while quartz keeps stable, leading to the increasing contents of quartz and clay minerals.

(2) Rubidium is primarily hosted in K-bearing minerals (e.g., orthoclase and illite), while Sr is mainly hosted in Ca-rich minerals such as plagioclase and calcite. Therefore, the Rb/Sr ratio will increase during the weathering of Ca-bearing minerals (Chen et al., 2017). In Figure 6A, the Rb/Sr ratio in the mudstone section is notably higher than in the sandstone section, indicating the removal of plagioclase and calcite (Figures 5C, E) and suggesting strong weathering (Chang et al., 2013).

(3) Feldspar is the main host mineral of Eu (Condie et al., 1995). Feldspar weathering results in significant negative Eu anomaly ($\frac{Eu}{Eu^*} = \frac{Eu}{\sqrt{Sm^*Gd}}$) in the parent rock (Vinnarasi et al., 2020). During the calculation, the chondrite data were used for normalization (Taylor and Mclennan, 1985). As shown in Figure 5C, the feldspar content always decreased from bottom to top in the profile, consistent with Figure 6B, in which the positive Eu anomalies (>1) in the sandstone section against the negative Eu anomalies (<1) in the mudstone section. These observations suggest the gradual removal of feldspar with the chemical weathering.

(4) The weathering of carbonate is often accompanied by significant rare earth element (REE) fractionation (Mao et al., 2017; Walter et al., 1995), such as La/Yb ratio can reflect the weathering intensity of carbonate (Rudnick et al., 1993). Indeed, Ji et al. (2004) attributed the obvious fractionation between light and heavy rare earth elements in red residua of Yunnan-Guizhou Plateau to the carbonate weathering. As shown in Figure 6C, the La/Yb ratio of this profile keeps constant at ~20, arguing against an important role of carbonate weathering. Moreover, the regional geology indicates that the provenance of the Yungang Formation was mainly derived from the surrounding Archean-Early Proterozoic metamorphic rocks, with minor carbonate components (Figure 2). In fact, the carbonate minerals are mainly produced as cement or secondary minerals in sandstones, and the mudstone section that contains a small amount of feldspar have rare carbonate minerals, so they are likely to represent the weathering products of feldspar. For example, the formation of calcite can be ascribed to interaction between the Ca ions produced through plagioclase decomposition and the dissolved atmospheric CO_2 (Amrhein and Suarez, 1992; Oelkers and Schott, 1995). Similar phenomena have also been observed in the Mogao Caves and the Bamiyan Buddha (Ye et al., 2016; Margottini, 2007). Previous studies have also demonstrated that calcite dissolution within feldspar sandstone matrices is significantly inhibited (Yuan et al., 2015). Therefore, we consider that the contribution of carbonate weathering is minor during the chemical weathering of the sandstones in the grottoes.

(5) Previous studies have also reported the existence of sulphate minerals such as gypsum on the surface of some grottoes (Ma et al., 2005). These minerals likely represent the products of wet deposition via the dissolution of atmospheric SO_2 onto the calcite, the specific reaction equations are shown in Formula 4–6 (Gomez-Heras and McCabe, 2015; Qin et al., 2016).

$$2SO_2 + O_2 = 2SO_3 \quad (4)$$

$$SO_3 + H_2O = H_2SO_4 \quad (5)$$

$$CaCO_3 + H_2SO_4 + H_2O = CaSO_4 \cdot 2H_2O\,(\text{gypsum}) + CO_2\uparrow \quad (6)$$

However, almost no sulphate has been identified in our studied samples from the Shiku Member profile, suggesting that the role of acid rainfall was insignificant during the chemical weathering of the sandstones. Possible reasons include: (1) the road was built when the atmospheric SO_2 was at low levels, and/or (2) the mudstone section acted as a shielding layer and blocked the penetration of acid rainfall into the sandstone section.

3.4 Chemical weathering rate of the Yungang Grottoes

It has been well acknowledged that temperature and pH significantly influence the feldspar dissolution rate (Bastien et al., 2016; Ponziani et al., 2012; Zhou et al., 2023). To quantify their impacts, several equations have been proposed to calculate the dissolution rate, including the linear transition state theory (L-TST) rate law (Aagaard and Helgeson, 1982), the nonlinear transition state theory (TST) rate law (Steefel and Cappellen, 1990), the parallel rate equation (Burch et al., 1993), the rate law of the step wave model (Lasaga and Luttge, 2001), and the partial equilibrium law (Crundwell, 2015a; Crundwell, 2015b). Considering that reactions typically occur far from equilibrium under natural conditions, we adapt the L-TST rate equation (Equation 7) to estimate the dissolution rate of feldspar:

$$r_m = k_m \cdot A \cdot (a_{H^+})^{n_m} \cdot \left[1 - \exp\left(\frac{\Delta G_m}{\sigma R T}\right)\right] \quad (7)$$

In this equation, m is the mineral index. In this paper, we do not consider anorthite to be a major phase during chemical weathering of the Yungang Grottoes, as indicated by petrographic observations, so m represents only albite and K-feldspar. r_m expresses the chemical weathering rate (mol·cm^{-2}·s^{-1}), k_m denotes the reaction rate constant at temperature T (mol·cm^{-2}·s^{-1}), A represents the specific surface area (cm^2/g), a_{H^+} signifies the hydrogen ion activity, and n is the empirical reaction order. In this study, the reaction order of albite is 0.572, that of K-feldspar is 0.823 (Palandri and Kharaka, 2004), ΔG_m is the change in the Gibbs free energy (kJ·mol^{-1}) of the reaction, and σ stands for the Temkin's average stoichiometric number (Matylda et al., 2022). In the dissolution reaction of albite and potassium feldspar, Temkin's number is 3 because in 1 mol of albite and K-feldspar, the stoichiometric coefficient of Si is 3 (Matylda et al., 2022). R is the gas constant with a value of 8.314 J/kcal·mol, and T is the Kelvin temperature.

k_m can usually be calculated according to the reaction rate constant at 25°C under far-from-equilibrium conditions and the

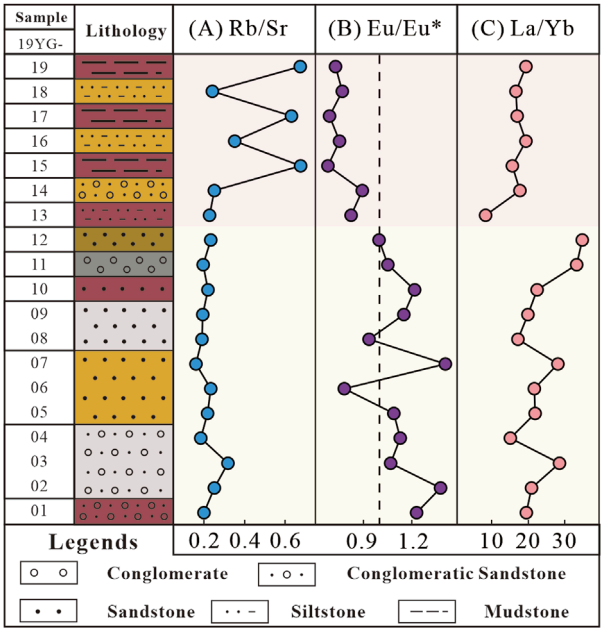

FIGURE 6
Elemental ratio variations in the profile. **(A)** Rb/Sr, **(B)** Eu/Eu∗and **(C)** La/Yb of the Shiku Member.

derivation of the van't Hoff Equation 8:

$$k_m = \mathrm{k}_{25,\mathrm{m}} \cdot \exp\left[\frac{-Ea_m}{\mathrm{R}}\left(\frac{1}{T} - \frac{1}{298.15}\right)\right] \quad (8)$$

$\mathrm{k}_{25,\mathrm{m}}$ is the reaction rate constant (mol·cm^{-2}·s^{-1}) at 25°C, and Ea_m is the activation energy (KJ/mol). During the calculation, the reaction rate constants of albite and K-feldspar are 1×10^{-15} mol·cm^{-2}·s^{-1} (Knaus and Wolery, 1986) and 1×10^{-16} mol·cm^{-2}·s^{-1} (from the PHREEQC thermodynamic database), respectively. The activation energies of albite and orthoclase used in the calculations under alkaline conditions are 71 kJ/mol and 94.1 kJ/mol, respectively (Palandri and Kharaka, 2004; Yuan et al., 2019).

A can be calculated using Formula 9 proposed by Brantley and Mellott (2000):

$$\mathrm{Log}\left(A, \mathrm{cm}^2 \cdot \mathrm{g}^{-1}\right) = b + m \cdot \log(d) \quad (9)$$

In Equation 9, $b = 5.2 \pm 0.2$, $\mathrm{m} = -1.0 \pm 0.1$, and d is the particle diameter (μm).

According to the Gibbs free energy equation, ΔG_m is:

$$\Delta G_m = \Delta H_m - T \cdot \Delta S_m \quad (10)$$

Here, ΔH_m represents the standard molar enthalpy of formation (KJ/mol), T represents the Kelvin temperature, and ΔS_m signifies the standard molar entropy of formation (J/Kcal·mol). According to thermodynamic data (Huang et al., 2009), the $\Delta \mathrm{H}_{\mathrm{Ab}}$ of the albite dissolution reaction is −77.57 kJ/mol, the $\Delta \mathrm{S}_{\mathrm{Ab}}$ is 0.91 J/kcal·mol, and the $\Delta \mathrm{H}_{\mathrm{Or}}$ and $\Delta \mathrm{S}_{\mathrm{Or}}$ of the K-feldspar dissolution reaction are −21.52 kJ/mol and 1.27 J/kcal·mol, respectively.

Combining Equations 8–10, we can obtain the chemical weathering rate:

$$\begin{aligned} \mathrm{r} = {} & \alpha_{\mathrm{Ab}} \cdot \mathrm{k}_{25,\mathrm{Ab}} \cdot \exp\left[\frac{-\mathrm{Ea}_{\mathrm{Ab}}}{\mathrm{R}}\left(\frac{1}{T} - \frac{1}{298.15}\right)\right] \cdot A \cdot (a_{H^+})^{n_{Ab}} \\ & \cdot \left[1 - \exp\left(\frac{\Delta \mathrm{H}_{\mathrm{Ab}} - T\Delta \mathrm{S}_{\mathrm{Ab}}}{\sigma \mathrm{R}T}\right)\right] + \left(1 - \alpha_{\mathrm{Ab}}\right) \cdot \mathrm{k}_{25,\mathrm{Or}} \\ & \cdot \exp\left[\frac{-\mathrm{Ea}_{\mathrm{Or}}}{\mathrm{R}}\left(\frac{1}{T} - \frac{1}{298.15}\right)\right] \cdot A \cdot (a_{H^+})^{n_{Or}} \cdot \left[1 - \exp\left(\frac{\Delta \mathrm{H}_{\mathrm{Or}} - T\Delta \mathrm{S}_{\mathrm{Or}}}{\sigma \mathrm{R}T}\right)\right] \end{aligned} \quad (11)$$

The α_{Ab} is the proportion of the albite component.

Previous studies have demonstrated notable discrepancies in feldspar dissolution rate between laboratory and field conditions, which are attributed to variables such as temperature, pH, and mineral surface reactivity (Gruber et al., 2014; Reeves and Rothman, 2013; White and Brantley, 2003). To address these variations, all parameters employed in this study were exclusively derived from site-specific data of the Yungang Grottoes. Although thermodynamic parameters originate from laboratory measurements, they represent intrinsic characteristics and are thus independent of experimental or natural conditions. For instance, based on the sandstone composition of the grottoes, characterized by particle sizes ranging from 0.063 to 2 mm, we calculated a specific surface area of 153.71 cm^2/g using Equation 9. Field data collection focused on the hydrogeochemical parameters in the Datong region during 2022. The temperature in Yungang area ranged from 255.65 K (−17.5°C) to 301.15 K (28.0°C), with a mean value of 280.75 K (7.6°C). The pH of groundwater changed little, with the lowest pH of 7.91 and an average pH of 8.23. Detailed groundwater pH and temperature profiles are presented in Figure 7 (Panels A and B, respectively), with complete datasets archived in Supplementary Table S2. The shaded colorful fields in Figures 7, 8 represent the calculation error bars, which are derived from the difference between the average temperature and the maximum or minimum of multiple measured values per day; and they are same for the pH value of groundwater (one measurement for every 4 h).

According to Formula 11, we explored the relationships between chemical weathering rate and pH and temperature (Figure 7). In Figure 7C, the average temperature of 280.75 K is fixed to show the influence of pH on the chemical weathering of feldspar. The pH shows a mirror relationship with the chemical weathering rate of feldspar, with the lowest pH (7.91) corresponding to the highest weathering rate (3.43×10^{-19} mol·cm^{-2}·s^{-1}) and the highest pH (8.51) corresponding to the lowest weathering rate (1.55×10^{-19} mol·cm^{-2}·s^{-1}). In Figure 7D, the average pH (8.23) is fixed to show the influence of temperature. A positive correlation exists between the chemical weathering rate and temperature, with the highest temperature of 301.15 K (28.0°C) corresponding to the highest weathering rate (1.78×10^{-18} mol·cm^{-2}·s^{-1}) and the lowest temperature of 255.65 K (−17.5°C) corresponding to the lowest weathering rate (1.14×10^{-20} mol·cm^{-2}·s^{-1}). Our calculation results agree with prior studies on feldspar-fluid interactions, indicating that an increase in temperature elevates the fraction of activated molecules, while a decrease in pH enhances the availability of H^+, thereby facilitating the reaction (Bastien et al., 2016; Zhou et al., 2023).

The chemical weathering rate of feldspar caused by the temperature change is much greater than that caused by the pH shift (Figures 7C,D). When the pH changed (Figure 7C), the maximum (3.43×10^{-19} mol·cm^{-2}·s^{-1}) and minimum (1.55×10^{-19} mol·cm^{-2}·s^{-1}) weathering rates were only about 2 times different. While, when the temperature changes (Figure 7D), the maximum chemical weathering rate is 1.78×10^{-18} mol·cm^{-2}·s^{-1}, the minimum chemical value is 1.14×10^{-20} mol·cm^{-2}·s^{-1}, and the difference is approximately 150 times greater. In the Shiku Member (lithostratigraphic unit), the effect of temperature on the chemical weathering rate is more obvious than that of pH. This difference in weathering rate is probably attributed to the greater variation in temperature than in groundwater pH (Figures 7A, B).

The daily weathering amount (A_d, mol·cm^{-2}·day^{-1}) and annual cumulative weathering amount (A_c, mol·cm^{-2}·year^{-1}) are estimated by the following Equations 12, 13:

$$A_d = r \times 24 \times 60 \times 60 \quad (12)$$

$$A_c = \sum_{\mathrm{i}=1}^{365} r_i \times 24 \times 60 \times 60 \quad (13)$$

According to the calculation results (Figure 8A), the chemical weathering rate in summer is faster ($0.3–2.3 \times 10^{-13}$ mol·cm^{-2}·day^{-1}), while that in winter is the lowest (close to 0). The chemical weathering rate in spring and autumn is moderate, ranging from $0.1–0.3 \times 10^{-13}$ mol·cm^{-2}·day^{-1}.

The cumulative weathering amount (Figure 8B) can more intuitively reflect the chemical weathering process within a year.

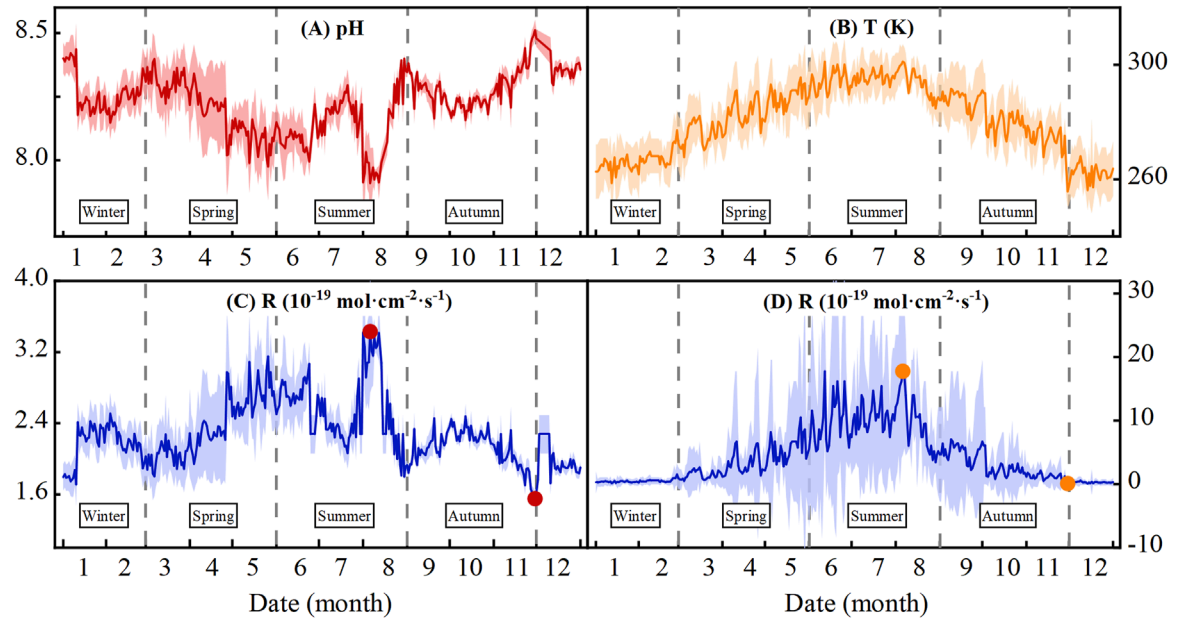

FIGURE 7
Variations in **(A)** pH and **(B)** T (temperature, K) in the Datong area, North China, 2022 and the calculated chemical weathering rates caused by **(C)** pH change and **(D)** T change. The solid circles in **(C, D)** represent the extreme values.

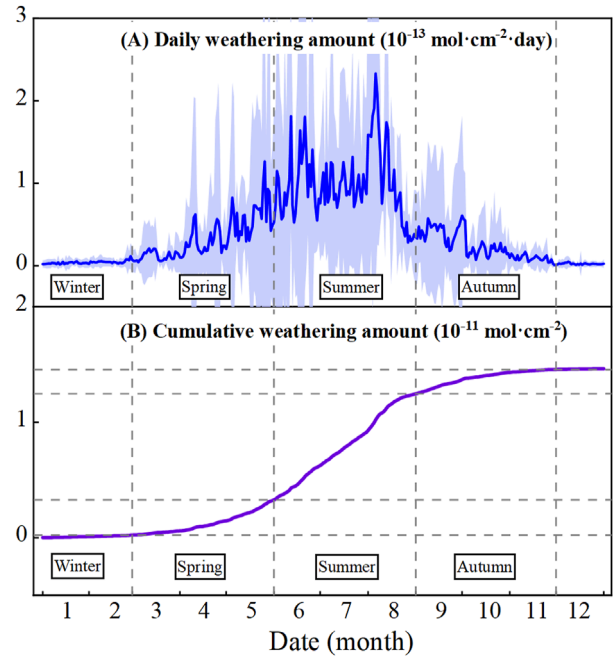

FIGURE 8
Diagrams showing the **(A)** daily and **(B)** cumulative annual chemical weathering amounts in the Datong area, North China during 2022.

In spring and autumn, the cumulative weathering amount is about 0.2–0.3 × 10^{-11} mol/cm^2, while in summer, it reaches around 9.2 × 10^{-12} mol/cm^2. The weathering amount in summer accounts for approximately 62.8% of the annual weathering value.

3.5 Implications for the protection of Yungang Grottoes

It is crucial to determine the chemical weathering rate that helps estimate the timescale for structural damage of the Yungang Grottoes when protective measures are absent. The annual percentage of chemical weathering can be calculated by R_c with the following formula:

$$\eta = 100 \times R_c \cdot A \cdot (\alpha_{Ab} \cdot M_{Ab} + \alpha_{Or} \cdot M_{or}) \quad (14)$$

Here, η represents the annual chemical weathering percentage; α represents the mineral component content, and M is the molar mass of the corresponding mineral. In accordance with Equation 14, the chemical weathering percentage of Yungang Grottoes in 2022 is approximately 0.000061%.

Although the roles of physical weathering processes, such as precipitation, cracks, dust deposits, black smoke, condensation water (Qin et al., 2016) and salt crystallization (Zhang et al., 2013), have been identified, whereas the quantitative evaluation of physical weathering on the Yungang Grottoes remains absent.

In accordance with the estimation method proposed by Gabet and Mudd (2009), there is a quantitative relationship of about 1.5–1.9 times between physical and chemical weathering in tectonically stable regions such as the Datong area, North China. Accordingly, we can estimate that the amount of weathering (chemical + physical weathering) of the Yungang Grottoes is approximately 0.00015%–0.00018%.

According to Cai (2022), when the mass loss ratio of sandstone reaches about 5%, cracks, collapses or block shedding begin to occur. Therefore, it may take approximately 300 years (=5% ÷ 0.00015%–0.00018% years) for the mass loss to reach 5%.

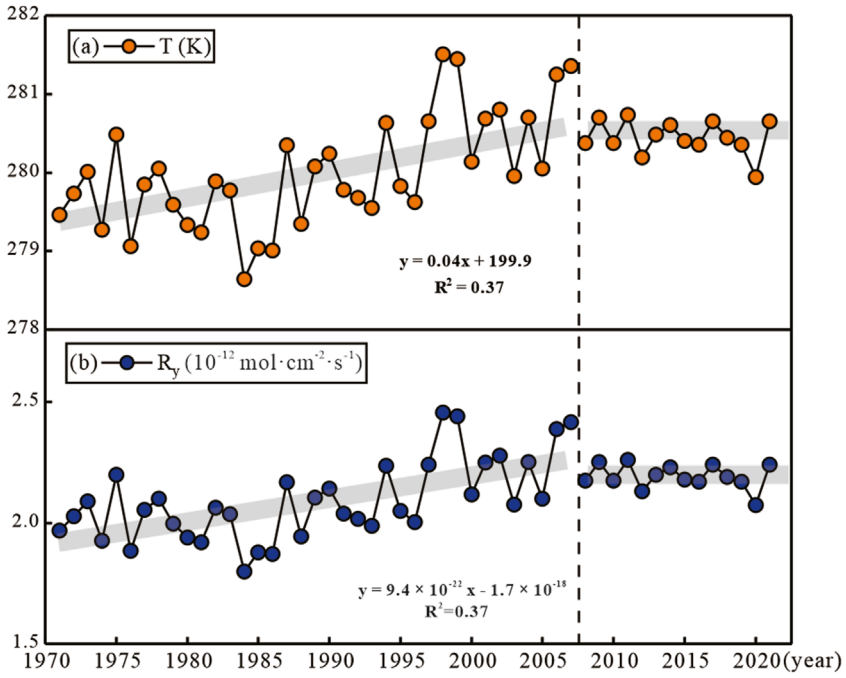

FIGURE 9
Annual average **(a)** temperatures and **(b)** chemical weathering rates from 1971 to 2021.

Assuming that the initial construction of the Yungang Grottoes occurred 1,500 years ago (AD 450–520), the carved sandstones were fresh; if no protective measures and/or artificial destruction were applied, the Yungang Grottoes began to destruct in ca. AD 800 (equivalent to the Tang Dynasty). Moreover, the Yungang Grottoes will be destroyed in the coming 4,000–5,000 years (=100% ÷ 0.00015%–0.00018% - 1,500) under natural conditions.

We collected the annual average temperatures from 1971 to 2021 in the Datong area (Figure 9a) (He, 2011). The results show an increasing annual average temperature after the onset of industrialization in China, with an increase of approximately 0.5°C per decade. Because of the implementation of energy conservation and emission reduction policies since 2007, the annual average temperature kept relatively stable in recent years. At the same time, the stable pH value of groundwater is also likely to be related to the low level of SO_2 content in the air after these policies (Xuan et al., 2021; Zhang et al., 2023). As shown in Figure 9, the continuous increase in annual average temperature also accelerates the weathering rate, leading to more rapid structural and morphological damage of the grottoes during 1971–2007.

Collectively, it is essential to specifically address temperature fluctuations before protective measures are implemented to reduce weathering intensity at the Yungang Grottoes. If possible, we should reduce the impact of extreme temperature fluctuations on the grottoes by controlling the surrounding temperature. For example, we can use air conditioners to stabilize the ambient temperature. Alternatively, we can reduce direct exposure to sunlight by constructing shading structures or planting trees, which may lower surface temperature fluctuations. We may also apply appropriate protective coatings to the surface of the grottoes to help mitigate the impact of temperature changes on the interior. Regular monitoring of temperature changes inside and outside the grottoes will help to adjust protective measures. Raising awareness of environmental protection among the public and tourists will also reduce unnecessary human-induced temperature fluctuations. Finally, reducing carbon emission is also significant to decrease annual chemical weathering rate and to decelerate the damage of stone cultural relics (Figure 9).

4 Conclusion

Our geochemical analyses on the Shiku Member (lithostratigraphic unit) show that the chemical weathering rate of the Yungang Grottoes are dominated by feldspar dissolution, whereas the roles of calcite and sulphate recrystallization are minor. Considering the effects of physical weathering such as precipitation, condensation water and cracks, we calculate the total weathering rate and cumulative weathering amount of the Yungang Grottoes, which provide a new approach to estimating the life of these stone heritages and further protection measures. The following conclusions can be summarized.

1) The factors affecting the chemical weathering rate of the Yungang Grottoes include temperature and pH value. The weathering rate is positively correlated with temperature and inversely correlated with the pH of groundwater.
2) According to the present estimation, the structural damage of Yungang Grottoes began to occur ca. 300 years after building-up (ca. AD 800, equivalent to the Tang Dynasty), and will

be destroyed within the upcoming 4,000–5,000 years with no protective measure.

3) The predominant factor affecting the local chemical weathering rate is temperature. Addressing temperature fluctuations is therefore crucial for implementing protective measures aimed at reducing chemical weathering rate of the Yungang Grottoes. Planting trees, installing air conditioners, adding eaves and reducing cardon emission can effectively control the temperature shift of the grottoes.

While current estimations require refinement due to uncertainties in physical weathering intensity, our results provide a novel approach to quantitative assessment of weathering in the Yungang Grottoes.

Data availability statement

The original contributions presented in the study are included in the article/Supplementary Material, further inquiries can be directed to the corresponding author.

Author contributions

XH: Conceptualization, Data curation, Methodology, Visualization, Writing–original draft, Writing–review and editing. FG: Funding acquisition, Supervision, Writing–review and editing. LZ: Writing–review and editing. FZ: Writing–review and editing.

Funding

The author(s) declare that financial support was received for the research, authorship, and/or publication of this article. This study was financially supported by the National Natural Science Foundation of China (Grants 42,021,002, 42073032 and 41525006).

Acknowledgments

We greatly thank Wu Wenchang for technical help with the XRF and ICP-MS analyses, Hong Xiaofeng for the XRD analyses, and Yuan Guanghui for guiding chemical weathering rate calculation. Fruitful discussions with Profs. Xia Xiaoping, Ren Zhongyuan, Peng Touping, and Chen Jianlin helped clarify and improve the manuscript.

Conflict of interest

The authors declare that the research was conducted in the absence of any commercial or financial relationships that could be construed as a potential conflict of interest.

Generative AI statement

The author(s) declare that no Generative AI was used in the creation of this manuscript.

Publisher's note

Supplementary material

The Supplementary Material for this article can be found online at: https://www.frontiersin.org/articles/10.3389/feart.2025.1507580/full#supplementary-material

References

Aagaard, P., and Helgeson, H. C. (1982). Thermodynamic and kinetic constraints on reaction rates among minerals and aqueous solutions; I, Theoretical considerations. *Am. J. Sci.* 282 (3), 237–285. doi:10.2475/ajs.282.3.237

Ai, X., Chen, X., and Sun, B. (2021). Sedimentary features of fluvial facies in the shiku member of Yungang Formation in datong basin. *Sci. Technol. Eng.* 21 (9), 3495–3504. doi:10.3969/j.issn.1671-1815.2021.09.009

Amrhein, C., and Suarez, D. L. (1992). Some factors affecting the dissolution kinetics of anorthite at 25°C. *Geochim. Cosmochim. Acta* 56 (5), 1815–1826. doi:10.1016/0016-7037(92)90312-7

Bastien, W., Damien, D., François, G., Kevin, G. K., Marion, P.-V., and Gwenaël, I. (2016). pH-dependent control of feldspar dissolution rate by altered surface layers. *Chem. Geol.* 442, 148–159. doi:10.1016/j.chemgeo.2016.08.035

Becherini, F., Bernardi, A., and Frassoldati, E. (2010). Microclimate inside a semi-confined environment: valuation of suitability for the conservation of heritage materials. *J. Cult. Herit.* 11 (4), 471–476. doi:10.1016/j.culher.2010.01.005

Brantley, S. L., and Mellott, N. P. (2000). Surface area and porosity of primary silicate minerals. *Am. Mineral.* 85 (11-12), 1767–1783. doi:10.2138/am-2000-11-1220

Burch, T. E., Nagy, K. L., and Lasaga, A. C. (1993). Free energy dependence of albite dissolution kinetics at 80°C and pH 8.8. *Chem. Geol.* 105 (1-3), 137–162. doi:10.1016/0009-2541(93)90123-z

Cai, T. (2022). "Study on surface weathering mechanism of sandstone at Inner Mongolia Aerzhai grottoes," in *Master's thesis*. Lanzhou: Lanzhou university.

Camuffo, D. (1995). Physical weathering of stones. *Sci. Total Environ.* 167 (1-3), 1–14. doi:10.1016/0048-9697(95)04565-i

Chang, H., An, Z. J., Wu, F., Jin, Z. D., Liu, W. G., and Song, Y. G. (2013). A Rb/Sr record of the weathering response to environmental changes in westerly winds across the Tarim Basin in the late Miocene to the early Pleistocene. *Palaeogeogr. Palaeoclimatol. Palaeoecol.* 386, 364–373. doi:10.1016/j.palaeo.2013.06.006

Chen, J., An, Z., and Head, J. (2017). Variation of Rb/Sr ratios in the loess-paleosol sequences of Central China during the last 130,000 Years and their implications for monsoon paleoclimatology. *Quat. Res.* 51 (3), 215–219. doi:10.1006/qres.1999.2038

Condie, K. C., Dengate, J., and Cullers, R. L. (1995). Behavior of rare earth elements in a paleoweathering profile on granodiorite in the Front Range, Colorado, USA. *Geochim. Cosmochim. Acta* 59 (2), 279–294. doi:10.1016/0016-7037(94)00280-y

Crundwell, F. K. (2015a). The mechanism of dissolution of the feldspars: Part I. Dissolution at conditions far from equilibrium. *Hydrometallurgy* 151, 151–162. doi:10.1016/j.hydromet.2014.10.006

Crundwell, F. K. (2015b). The mechanism of dissolution of the feldspars: Part II dissolution at conditions close to equilibrium. *Hydrometallurgy* 151, 163–171. doi:10.1016/j.hydromet.2014.10.004

Fan, W., Guo, F., Wang, Y., and Zhang, M. (2004). Late Mesozoic volcanism in the northern Huaiyang tectono-magmatic belt, central China: partial melts from a lithospheric mantle with subducted continental crust relicts beneath the Dabie orogen? *Chem. Geol.* 209 (1-2), 27–48. doi:10.1016/j.chemgeo.2004.04.020

Fan, X., Wang, H., Ai, X., Yang, F., and Wang, K. (2014). Study on characteristics of sedimentary facies of shiku member of Yungang formation in datong basin Inner Mongolia Petrochem. *Ind* 19, 123–129. doi:10.3969/j.issn.1006-7981.2014.19.050

Frost, B. R., and Lindsley, D. H. (1991). "Chapter 12.Occurrence of iron-titanium oxides in igneous rocks," in *Oxide minerals*. Editor H. L. Donald (Berlin, Boston: De Gruyter), 433–468.

Fu, Q., Lu, P., Konishi, H., Dilmore, R., Xu, H., Jr., Zhu, C., et al. (2009). Coupled alkali-feldspar dissolution and secondary mineral precipitation in batch systems: 1. New experiments at 200 °C and 300 bars. *Chem. Geol.* 258 (3-4), 125–135. doi:10.1016/j.chemgeo.2008.09.014

Gabet, E. J., and Mudd, S. (2009). A theoretical model coupling chemical weathering rates with denudation rates. *Geology* 37 (2), 151–154. doi:10.1130/g25270a.1

Gomez-Heras, M., and McCabe, S. (2015). Weathering of stone-built heritage: a lens through which to read the Anthropocene. *Anthropocene* 11, 1–13. doi:10.1016/j.ancene.2015.12.003

Gong, Q., Deng, J., Yang, L., Zhang, J., Wang, Q., and Zhang, G. (2011). Behavior of major and trace elements during weathering of sericite–quartz schist. *J. Asian Earth Sci.* 42 (1-2), 1–13. doi:10.1016/j.jseaes.2011.03.003

Gong, Q., Zhou, L., Hu, Y., Yan, L., Zhang, H., and Jia, Y. (2012). Element transfer behaviors and its application during lamprophyre alteration in the linglong gold deposit, jiaodong peninsula, China. *Geoscience* 26 (5), 1065–1077. doi:10.3969/j.issn.1000-8527.2012.05.028

Gruber, C., Harpaz, L., Zhu, C., Bullen, T., and Ganor, J. (2014). A new approach for measuring dissolution rates of silicate minerals by using silicon isotopes. *Geochim. Cosmochim. Acta* 104, 261–280. doi:10.1016/j.gca.2012.11.022

Guidry, M. W., and Mackenzie, F. T. (2000). Apatite weathering and the Phanerozoic phosphorus cycle. *Geology* 28 (7), 631–634. doi:10.1130/0091-7613(2000)28<631:Awatpp>2.0.Co;2

Guo, F., and Jiang, G. (2014). Investigation into rock moisture and salinity regimes: implications of sandstone weathering in Yungang Grottoes, China. *Carbonates Evaporites* 30 (1), 1–11. doi:10.1007/s13146-014-0191-8

Guo, H., and Bai, B. (2024). Cultural inheritance and application of Yungang grottoes statues in art education. *Arts Educ.*, 311–343.

He, Z. (2011). Characteristics of extreme temperature change nearly 40 Years in datong. *Chin. J. Agrometeorol.* 32, 15–18.

Hogarth, D. D., and Robin, M. J. L. (2007). Strontium in feldspars of high-K proterozoic igneous rocks of the robitaille suite, buckingham, quebec. *Can. Mineral.* 45 (5), 1293–1306. doi:10.2113/gscanmin.45.5.1293

Huang, J., and Zhang, J. (1998). Application of electrical prospecting to investigate rock mass cracks in Yungang Grottoes. *World Antiq.* (3), 86–90.

Huang, J., Zheng, Y., and Li, H. (2022). Study of internal moisture condensation for the conservation of stone cultural heritage. *J. Cult. Herit.* 56, 1–9. doi:10.1016/j.culher.2022.05.003

Huang, K., Huang, S., Tong, H., and Liu, L. (2009). Thermodynamic calculation of feldspar dissolution and the significance on research of clastic reservoir. *Geol. Bull. China.* 28 (4), 474–482. doi:10.3969/j.issn.1671-2552.2009.04.008

Huang, S., and Yang, J. (1995). Exeprimental study of feldspar dissolution by acetic acid at different burial temperatures. *Acta Sedimentol. Sin.* 13 (1), 7–17. doi:10.14027/j.cnki.cjxb.1995.01.002

Ji, H., Wang, S., Ouyang, Z., Zhang, S., Sun, C., Liu, X., et al. (2004). Geochemistry of red residua underlying dolomites in karst terrains of Yunnan-Guizhou Plateau. *Chem. Geol.* 203 (1-2), 29–50. doi:10.1016/j.chemgeo.2003.08.013

Knaus, K. G., and Wolery, T. J. (1986). Dependence of albite dissolution kinetics on pH and time at 25°C and 70°C. *Geochim. Cosmochim. Acta* 50, 2481–2497. doi:10.1016/0016-7037(86)90031-1

Kovach, V. P., Samsonov, A. V., Kotov, A. B., Salnikova, E. B., Adamskaya, E. V., Bortnikov, V. V., et al. (2023). Arkose sandstones of the kebekta group of the ugui graben (aldan shield): age, provenance, and deposition setting. *Earth Sci.* 512 (1), 779–785. doi:10.1134/S1028334X23600998

Lasaga, A. C., and Luttge, A. (2001). Variation of crystal dissolution rate based on a dissolution stepwave model. *Science* 291 (5512), 2400–2404. doi:10.1126/science.1058173

Li, H., Wang, W., Zhan, H., Qiu, F., Guo, Q., and Zhang, G. (2014). Water in the Mogao Grottoes, China: where it comes from and how it is driven. *J. Arid. Land* 7 (1), 37–45. doi:10.1007/s40333-014-0072-y

Li, S., Huo, R., Wang, B., Ren, Z., Ding, Y., Qian, M., et al. (2018). Experimental study on physicomechanical properties of sandstone under acidic environment. *Adv. Civ. Eng.* 2018 (1). doi:10.1155/2018/5784831

Li, S., Huo, R., Yoshiaki, F., Ren, D., and Song, Z. (2019). Effect of acid-temperature-pressure on the damage characteristics of sandstone. *Int. J. Rock Mech. Min. Sci.* 122, 104079. doi:10.1016/j.ijrmms.2019.104079

Little, M. G., and Lee, C. A. (2006). On the formation of an inverted weathering profile on Mount Kilimanjaro, Tanzania: buried paleosol or groundwater weathering. *Chem. Geol.* 235 (3-4), 205–221. doi:10.1016/j.chemgeo.2006.06.012

Liu, R. Z., Zhang, B. J., Zhang, H., and Shi, M. F. (2011). Deterioration of Yungang grottoes: diagnosis and research. *J. Cult. Herit.* 12 (4), 494–499. doi:10.1016/j.culher.2011.03.008

Liu, Y., Liu, H., and Li, X. (1996). Simultaneous and precise determination of 40 trace elements in rock samples using ICP-ms. *Geochimiaca*, 552–558.

Ma, Z., Huang, J., and Zhang, H. (2005). Chemical weathering of carbonate cement in sandstone and the related cultural relic diseases in Yungang grottoes. Car. *Sin.* 24 (1), 71–76. doi:10.3969/j.issn.1001-4810.2005.01.011

Mao, G., Wei, G., Ma, J., Zeng, T., and Liu, Z. (2017). Mobilization and re-distribution of major and trace elements during the process of moderate weathering of carbonates in northern Guangdong, South China. *Geochimica* 46 (1), 33–45. doi:10.3969/j.issn.0379-1726.2017.01.004

Margottini, C. (2007). "Engineering geology and cultural heritage: the conservation of remaining Bamiyan Buddhas (Central Afghanistan)," in *Progress in landslide science*. Editors K. Sassa, H. Fukuoka, F. Wang, and G. Wang (Cham: Springer), 319–346.

Matylda, H., Voigt, M. J., Marieni, C., Julien, D., and Oelkers, E. H. (2022). A comprehensive and internally consistent mineral dissolution rate database: Part I: primary silicate minerals and glasses. *Chem. Geol.* 597, 120807. doi:10.1016/j.chemgeo.2022.120807

McLennan, S. M., Hemming, S., McDaniel, D. K., and Hanson, G. N. (1993). "Geochemical approaches to sedimentation, provenance, and tectonics," in *Processes controlling the composition of clastic sediments*. Editors M. J. Johnsson, and A. Basu (Boulder: Geological Society of America), 21–40.

Ndjigui, P. D., Bilong, P., Bitom, D., and Dia, A. (2008). Mobilization and redistribution of major and trace elements in two weathering profiles developed on serpentinites in the Lomié ultramafic complex, South-East Cameroon. *J. Afr. Earth Sci.* 50 (5), 305–328. doi:10.1016/j.jafrearsci.2007.10.006

Nesbitt, H. W., and Young, G. M. (1982). Early Proterozoic climates and plate motions inferred from major element chemistry of lutites. *Nature* 299, 715–717. doi:10.1038/299715a0

Ng, C. W. W., Guan, P., and Shang, Y. J. (2001). Weathering mechanisms and indices of the igneous rocks of Hong Kong. *Q. J. Eng. Geol. Hydrogeol.* 34 (2), 133–151. doi:10.1144/qjegh.34.2.133

Oelkers, E. H., and Schott, J. (1995). Experimental study of anorthite dissolution and the relative mechanism of feldspar hydrolysis. *Geochim. Cosmochim. Acta* 59 (24), 5039–5053. doi:10.1016/0016-7037(95)00326-6

Palandri, J. L., and Kharaka, Y. K. (2004). *A compilation of rate parameters of water-mineral interaction kinetics for application to geochemical modeling*. Menlo Park, CA: U.S. Geological Survey.

Paradise, T. R. (2002). Sandstone weathering and aspect in Petra, Jordan. *Z. Geomorphol.* 46 (1), 1–17. doi:10.1127/zfg/46/2002/1

Pokrovsky, O. S., Schott, J., and Dupre´, B. (2006). Trace element fractionation and transport in boreal rivers and soil porewaters of permafrost-dominated basaltic terrain in Central Siberia. *Geochim. Cosmochim. Acta* 70 (13), 3239–3260. doi:10.1016/j.gca.2006.04.008

Ponziani, D., Ferrero, E., Appolonia, L., and Migliorini, S. (2012). Effects of temperature and humidity excursions and wind exposure on the arch of Augustus in Aosta. *J. Cult. Herit.* 13 (4), 462–468. doi:10.1016/j.culher.2012.01.005

Qin, Y., Wang, Y., Li, L., and Huang, J. (2016). Experimental weathering of weak sandstone without direct water participation by using sandstone from the Yungang grottoes in datong, China. *Rock Mech. Rock Eng.* 49 (11), 4473–4478. doi:10.1007/s00603-016-1003-3

Reeves, D., and Rothman, D. H. (2013). Age dependence of mineral dissolution and precipitation rates. *Glob. Biogeochem. Cycles* 27, 906–919. doi:10.1002/gbc.20082

Ren, J., Huang, J., Meng, T., Wang, X., and Hu, c. (2019). Non-destructive evaluation of weathering degree of columns in No.9 and 10 cave of Yungang Grottoes with environmental magnetic meter. *Geotech. Investig. Surv.* 47 (7), 73–78.

Riebe, C. S., Kirchner, J. W., and Finkel, R. C. (2003). Long-term rates of chemical weathering and physical erosion from cosmogenic nuclides and geochemical mass balance. *Geochim. Cosmochim. Acta* 67 (22), 4411–4427. doi:10.1016/s0016-7037(03)00382-x

Rudnick, R. L., McDonough, W. F., and Chappell, B. W. (1993). Carbonatite metasomatism in the northern Tanzanian mantle: petrographic and geochemical characteristics. *Earth Planet. Sci. Lett.* 114 (4), 463–475. doi:10.1016/0012-821x(93)90076-l

Shao, L., Fielding, C., Mu, G., Lu, J., Zhang, P., Li, Y.-n., et al. (2024). "Coal accumulation patterns and paleoclimates in a carboniferous–permian cratonic basin, North China," in *Field trip guidebook on Chinese sedimentary geology*. Editor X. M. Hu (Guangzhou: Guangzhou Institute of Geochemistry), 231–357.

Shotyk, W., Weiss, D., Kramers, J. D., Frei, R., Cheburkin, A. K., Gloor, M., et al. (2001). Geochemistry of the peat bog at Etang de la Gruère, Jura Mountains, Switzerland, and its record of atmospheric Pb and lithogenic trace metals (Sc, Ti, Y, Zr, and REE) since 12,370 14 C yr BP. *Geochim. Cosmochim. Acta* 65 (14), 2337–2360. doi:10.1016/s0016-7037(01)00586-5

Steefel, C. I., and Cappellen, P. V. (1990). A new kinetic approach to modeling water-rock interaction: the role of nucleation, precursors, and Ostwald ripening. *Geochim. Cosmochim. Acta* 54 (10), 2657–2677. doi:10.1016/0016-7037(90)90003-4

Taherynia, M. H., Aghda, S. M. F., and Fahimifar, A. (2016). *In-Situ* stress state and tectonic regime in different depths of earth crust. *Geotech. Geol. Eng.* 34 (2), 679–687. doi:10.1007/s10706-016-9978-9

Taylor, S. R., and Mclennan, S. M. (1985). The continental crust: its composition and evolution Oxford: Blackwell Scientific Publications, 312.

Vinnarasi, F., Srinivasamoorthy, K., Saravanan, K., Gopinath, S., Prakash, R., Ponnumani, G., et al. (2020). Rare earth elements geochemistry of groundwater from Shanmuganadhi, Tamilnadu, India: chemical weathering implications using geochemical mass-balance calculations. *Geochemistry* 80 (4), 125668. doi:10.1016/j.chemer.2020.125668

Vlcko, J., Greif, V., Grof, V., Jezny, M., Petro, L., and Brcek, M. (2009). Rock displacement and thermal expansion study at historic heritage sites in Slovakia. *Environ. Geol.* 58 (8), 1727–1740. doi:10.1007/s00254-008-1672-7

Walter, A. V., Nahon, D., Flicoteaux, R., Girard, J. P., and Melfi, A. (1995). Behaviour of major and trace elements and fractionation of REE under tropical weathering of a typical apatite-rich carbonatite from Brazil. *Earth Planet. Sci. Lett.* 136 (3-4), 591–602. doi:10.1016/0012-821x(95)00195-i

Wang, X., Wan, L., Huang, J., Cao, W., Xu, F., and Dong, P. (2014). Variable temperature and moisture conditions in Yungang Grottoes, China, and their impacts on ancient sculptures. *Environ. Earth Sci.* 72 (8), 3079–3088. doi:10.1007/s12665-014-3213-x

Warscheid, T., and Braams, J. (2000). Biodeterioration of stone: a review. *Int. Biodeterior. Biodegr.* 46 (4), 343–368. doi:10.1016/s0964-8305(00)00109-8

Wei, X., Shi, X., Xu, Y., Castillo, P. R., Zhang, Y., Zhang, L., et al. (2022). Mid-Cretaceous Wake seamounts in NW Pacific originate from secondary mantle plumes with Arago hotspot composition. *Chem. Geol.* 587, 120632. doi:10.1016/j.chemgeo.2021.120632

Wen, Y., Guo, F., and Zhao, L. (2024). Origin of early triassic hornblende gabbro from the yunkai massif, south China: constraints from mineral and bulk-rock geochemistry. *Geosciences* 14 (6), 14060147. doi:10.3390/geosciences14060147

White, A. F., and Brantley, S. L. (2003). The effect of time on the weathering of silicate minerals: why do weathering rates differ in the laboratory and field? *Chem. Geol.* 202, 479–506. doi:10.1016/j.chemgeo.2003.03.001

Xia, J., Liu, H., Qiao, H., Zhu, L., and Liu, Y. (2024). A study for the distribution characteristics of surface temperature and the protection of grotto temples in China. *Environ. Monit. Assess.* 196 (12), 1248. doi:10.1007/s10661-024-13444-x

Xuan, C., Xiaoran, S., Zhaoji, S., Jiaen, Z., Zhong, Q., Huimin, X., et al. (2021). Analysis of the spatio-temporal changes in acid rain and their causes in China (1998–2018). *J. Resour. Ecol.* 12 (5), 593–599. doi:10.5814/j.issn.1674-764x.2021.05.002

Yan, H., Huang, J., Zhao, X., Hao, L., and Li, H. (2007). The temperature and humidity changes in Yungang grottoes and their influence to the caves′ conservation. *J. Shanxi Dat. Univ. Sci.* 23 (3), 25–29. doi:10.3969/j.issn.1674-0874.2007.03.009

Yang, X., Wang, J., Zhu, C., and He, M. (2018). Effect of water on long-term strength of column rocks based on creep behavior in Yungang grottoes, China. *Geotech. Geol. Eng.* 37 (1), 173–183. doi:10.1007/s10706-018-0601-0

Ye, F., Chen, W., Liang, X., Zhang, J., Guo, Z., and Guo, Q. (2016). Study on the weathering characteristics of the yumen glutenite in the Mogao grottoes in dunhuang. *J. Eng. Geol.* 24 (6), 1286–1293. doi:10.13544/j.cnki.jeg.2016.06.031

Yuan, G., Cao, Y., Jia, Z., Gluyas, J., Yang, T., Wang, Y., et al. (2015). Selective dissolution of feldspars in the presence of carbonates: the way to generate secondary pores in buried sandstones by organic CO_2. *Mar. Petrol. Geol.* 60, 105–119. doi:10.1016/j.marpetgeo.2014.11.001

Yuan, G., Cao, Y., Schulz, H.-M., Hao, F., Gluyas, J., Liu, K., et al. (2019). A review of feldspar alteration and its geological significance in sedimentary basins: from shallow aquifers to deep hydrocarbon reservoirs. *Earth-Sci. Rev.* 191, 114–140. doi:10.1016/j.earscirev.2019.02.004

Yuan, J., and Feng, X. (2004). Research on the weathering of Yungang grottoes. *World Antiq.* 5, 75–81. doi:10.3969/j.issn.1009-1092.2004.05.016

Zhang, H., Shi, M., Shen, W., Li, Z., Zhang, B., Liu, R., et al. (2013). Damage or protection? The role of smoked crust on sandstones from Yungang Grottoes. *J. Archaeol. Sci.* 40 (2), 935–942. doi:10.1016/j.jas.2012.09.031

Zhang, Y., Cao, C., Du, H., Huang, J., Guo, X., Luo, Q., et al. (2023). Investigation into the gaseous SO2 attack on sandstone in the Yungang grottoes. *Minerals* 13 (1), 13010123. doi:10.3390/min13010123

Zhang, Y., Zeng, J., and Yu, B. (2009). Experimental study on interaction between simulated sandstone and acidic fluid. *Petrol. Sci.* 6 (1), 8–16. doi:10.1007/s12182-009-0002-3

Zhang, Y., Zhang, Y., and Huang, J. (2022). Experimental study on capillary water absorption of sandstones from different grotto heritage sites in China. *Herit. Sci.* 10 (1), 25. doi:10.1186/s40494-022-00656-y

Zhou, R., Liu, D., Zhou, A., and Zou, Y. (2017). Provenance analyses of early Mesozoic sediments in the Ningwu basin: implications for the tectonic–palaeogeographic evolution of the northcentral North China Craton. *Int. Geol. Rev.* 61 (1), 86–108. doi:10.1080/00206814.2017.1407970

Zhou, S., Sun, Q., Zhang, H., Meng, H., Gao, Q., and Zhou, Y. (2023). Elemental dissolution characteristics of granite and gabbro under high-temperature water-rock interactions. *Sci. Total Environ.* 897, 165455. doi:10.1016/j.scitotenv.2023.165455